Numerical and experimental investigation on deterministic prediction of ocean surface wave and wave excitation force

I.-C. Kim, G. Ducrozet, Leroy Vincent, F. Bonnefoy, Y. Perignon, S. Delacroix

Applied Ocean Research 142 (2024) 103834

Contents lists available at ScienceDirect

Applied Ocean Research

journal homepage: www.elsevier.com/locate/apor

Research paper

Numerical and experimental investigation on deterministic prediction of ocean surface wave and wave excitation force

I.-C. Kim [a,b,*], G. Ducrozet [a], V. Leroy [a], F. Bonnefoy [a], Y. Perignon [a], S. Delacroix [a]

[a] Nantes Université, École Centrale Nantes, CNRS, LHEEA, UMR 6598, F-44000 Nantes, France
[b] College of Earth, Ocean, and Atmospheric Sciences, Oregon State University, Corvallis, OR, USA

ARTICLE INFO

Dataset link: https://doi.org/10.5281/zenodo.7689781

Keywords:
Wave excitation force
Ocean waves
Phase-resolved model
Real-time prediction
Directional wave
Wave tank experiments

ABSTRACT

Floating marine structures implement real-time wave excitation force prediction to address optimal control issues. The accuracy of force prediction relies on adequate wave forecasting. This paper presents a comprehensive analysis of deterministic wave forecasting by considering various wave steepnesses and directional spreads. In addition, we introduce new methods for predicting wave excitation forces acting on the floating body of interest. The methods are based on a set of frequency coefficients of wave excitation forces, which are generated in conjunction with wave amplitude parameters optimized in the data assimilation and frequency response functions obtained from boundary element method tools. These approaches offer the advantage of streamlining the calculation process, eliminating the need for simulating wave surfaces through wave propagation. Moreover, for the first time, we study a prediction zone for wave excitation forces by comparing predicted forces with theoretical forces. Lastly, the force prediction is validated against experiments conducted on a captive platform model in both unidirectional and multidirectional sea states.

1. Introduction

As one of the main renewable energy sources, ocean waves have the highest energy density and are therefore expected to be the most powerful energy carriers. In ocean wave energy harvesting systems, an active control strategy is required for wave energy converters, and information regarding wave excitation forces is crucial (Hals et al., 2011; Cretel et al., 2011; Fusco and Ringwood, 2012). Similarly, in the design of floating offshore wind turbines, several researchers have developed control strategies to mitigate turbine loads and increase power production based on knowledge of the wave excitation force from incoming waves (Raach et al., 2014; Ma et al., 2018; Al et al., 2020). The present work was conducted within the European H2020 FLOATECH and French ANR CREATIF projects.

Since the wave excitation force exerted on the floating structure cannot be accurately measured, several approaches have been suggested to estimate it. One approach is to measure the force by locking the structure at the position of interest. However, this experimental force is an approximation as it does not account for the displacement of the structure under the wave field (Hillis et al., 2020). Alternatively, the excitation force can be estimated using the frequency response function (FRF), which is obtained from the boundary element method (BEM) tools, such as NEMOH (Babarit and Delhommeau, 2015; Kurnia and Ducrozet, 2023), WAMIT (Lee and Newman, 2013), or their equivalents.

The inverse Fourier transform of the FRF, referred to as an impulse response function (IRF), is generally not causal. The concept of *non-causality* was introduced to characterize the input–output relationship at the center of the structure's water plane (e.g., Falnes, 1995; Guo et al., 2017; Al et al., 2020). The chosen input at a given instant t may not instantaneously cause the output. In other words, the excitation force at a given instant t depends on the future free surface elevation at the center of the structure's water plane. This non-causality can be attributed to the impacts of the wave hitting the floating structure and the generation of hydrodynamic pressure before reaching its center (Falnes, 1995). It was experimentally confirmed that the future wave prediction at the structure location from upstream measurements of the wave elevation is necessary to achieve current excitation forces at the time t (Bacelli et al., 2017).

A promising technique proposed to address this problem is based on X-band radar operating in the microwave regime, providing measurements of free surface elevations recorded from an onboard sensor for a large area of ocean surface wave field with directionality (e.g., Hilmer and Thornhill, 2015; Kusters et al., 2016; Naaijen et al., 2018; Klein et al., 2020; Zhang et al., 2022a). As an alternative, LIDAR (Light Detection and Ranging) cameras can acquire similar data sets of the ocean wave field (e.g., Grilli et al., 2011; Nouguier et al., 2013; Kabel et al.,

* Corresponding author.
E-mail address: inchul.kim@oregonstate.edu (I.-C. Kim).

https://doi.org/10.1016/j.apor.2023.103834
Received 13 July 2023; Received in revised form 3 October 2023; Accepted 4 December 2023
Available online 9 December 2023

2019; Desmars et al., 2020), but this technology currently has no commercial operating solutions. When structure-mounted cameras operate to obtain the wave fields surrounding the structure, the data measurements show physical limitations due to the grazing incidence angles of the cameras. To address these challenges, for example, to identify shadowed areas, the prediction algorithms have been developed based on spatio-temporal data sets of wave elevation (e.g., Grilli et al., 2011; Nouguier et al., 2013; Kabel et al., 2019; Desmars et al., 2020). At a later time, areas without measurements may become illuminated due to the wave motion.

Phase-resolved models accurately depict ocean wave prediction as they incorporate wave phase information, ensuring the capture of detailed surface wave dynamics. Nonlinear models have been employed for phase-resolved wave prediction because the nonlinear effects gradually become more significant over time or as the sea states become more severe, leading to a better description of wave field (Guérin et al., 2019). Floating platforms are generally designed to withstand all sea states over their life span, including extreme sea states with strong nonlinearity. Moreover, the wave energy converters are usually installed and function in severe sea states (Zhang et al., 2022b). In this regard, Nouguier et al. (2009) proposed the Choppy Wave Model (CWM) based on the Lagrangian approach to depict the instantaneous state of ocean wave motion. Subsequently, Guérin et al. (2019) developed the Improved Choppy Wave Model (ICWM), which allows for higher nonlinear wave dynamics while maintaining computational stability and efficiency. The Lagrangian model of a given order in wave steepness addresses more realistic physical features (e.g., wave statistics) compared to Eulerian developments of the same order (Pierson, 1961). Thus, Desmars et al. (2020) chose ICWM for deterministic wave prediction to achieve a good compromise between numerical stability, efficiency, and model accuracy.

Recently, Kim et al. (2023a) extended the wave prediction algorithms proposed by Desmars et al. (2020) to include directional sea states. They developed enhanced algorithms with simplified assimilation methods and optimal parameters and derived a three-dimensional spatial–temporal prediction zone within which the ocean surface is accurately predicted. To validate these algorithms, they conducted an experimental campaign using a network of wave gauges that mimicked the measurements of a LIDAR. The validating work involved sea states with different directional spreads but the same wave steepness.

In this study, we expand on the preliminary study by incorporating additional wave conditions with different wave steepnesses in both multidirectional and unidirectional sea states, entailing analysis of the effect of nonlinearity, in terms of wave steepness, on wave forecasting. Furthermore, we develop approaches to estimate the wave excitation force based on wave elevation predictions in both the frequency domain and the time domain. In the frequency domain, the wave parameters, which correspond to the initial wave and are optimized in the assimilation step, are used to construct the frequency-domain representation of the excitation force (Eqs. (20) and (23) being our main findings in this context.) Finally, we compare the wave force estimations to theoretical and experimental forces and discuss the wave excitation force prediction algorithms in terms of model accuracy, time prediction horizon, and applicability to multidirectional sea states. To the best of the authors' knowledge, the methods for wave excitation force prediction have not been previously applied in the context of directional wave fields. In particular, proper experimental validation of excitation force prediction under directional sea states has not been conducted.

The remainder of this paper is organized as follows. First, Section 2 details the prediction algorithms for wave excitation force as well as wave surface elevation. In particular, Section 2.3 deals with the approaches for excitation force modeling by means of wave amplitude parameters of wave models. Section 3 provides an overview of experimental campaigns aimed at simulating a situation where the camera is mounted on a structure and generates as many instantaneous measurements as the distance to the points with directionality. The numerical results for the wave excitation force estimations are validated against the dedicated experiments in Section 4. Finally, Section 5 presents the conclusions.

2. Real-time wave excitation force prediction

Real-time ocean wave forecasting is a two-step process: (1) data assimilation is a model initialization step from the observed wave field; (2) wave propagation simulates wave elevations by propagating forward in space and time. Next, the excitation force can be computed via a convolution integral between the predicted surface elevation $\eta(t)$ and the IRF $h(t)$ in the time domain (see Fig. 1(a)). Alternatively, a more straightforward method can be employed to provide the wave excitation force estimation on the basis of the frequency components, as shown in see Fig. 1(b). In this approach, the force component $F_{e,(n_\omega,n_\theta)}$ is obtained by combining wave amplitude parameters $a_{(n_\omega,n_\theta)}$, $b_{(n_\omega,n_\theta)}$, and the FRF $H_{(n_\omega,n_\theta)}$ (where n_ω and n_θ denote the n_ωth frequency component and the n_θth direction component, respectively). It is evident that there is an inconsistency when applying a linear transfer function in conjunction with the nonlinear wave predictions. However, we address this by incorporating nonlinear effects (e.g., Stokes drift) into the force component $F_{e,(n_\omega,n_\theta)}$ or the Fourier component for surface elevation $A_{\eta,(n_\omega,n_\theta)}$, which will be shown in Eq. (23). The details of the algorithms for force prediction are given in this section.

2.1. Wave models

We consider ICWM as the most mature tool equipped with several nonlinear features for data assimilation (or reconstruction; 'nowcast') and wave propagation (or prediction; 'forecast'). Two additional algorithms are developed in this study: one based on linear wave theory (LWT) and the other based on linear wave theory with a corrected dispersion relationship (LWT-CDR).

2.1.1. LWT

For the model based on LWT, the fluid is assumed to be inviscid and incompressible, and the flow is based on the assumption of irrationality. A three-dimensional wave field with ocean surface elevation at time t is represented by the linear wave theory over a Cartesian coordinate system $(x, y, z) = (\mathbf{r}, z)$, with z measured upwards from the still water level:

$$\begin{aligned}\eta^{\mathrm{LWT}}(x,y,t) &= \sum_{n=1}^{N}\left[a_n\cos\psi_n + b_n\sin\psi_n\right] \\ &= \sum_{n_\theta=1}^{N_\theta}\sum_{n_\omega=1}^{N_\omega}\left[a_{(n_\omega,n_\theta)}\cos\psi_{(n_\omega,n_\theta)} + b_{(n_\omega,n_\theta)}\sin\psi_{(n_\omega,n_\theta)}\right]\end{aligned} \tag{1}$$

where subscript n denotes the nth wave component, which can be redefined in frequency and direction as $n = (n_\omega, n_\theta)$. The total number of wave components is given by $N = N_\omega \times N_\theta$. The amplitude and the phase together determine the wave amplitude parameters (a_n, b_n), and the linear phase function is

$$\psi_n = \mathbf{k}_n\cdot\mathbf{r} - \omega_n t = k_{n_\omega}\cos\theta_{n_\theta}x + k_{n_\omega}\sin\theta_{n_\theta}y - \omega_{n_\omega}t \tag{2}$$

where $\mathbf{k}_n = k_{n_\omega}\hat{\mathbf{k}}_{n_\theta} = (k_{n_\omega}\cos\theta_{n_\theta}, k_{n_\omega}\sin\theta_{n_\theta})$ is the wavenumber vector and $\mathbf{r} = (x, y)$ is the horizontal coordinate vector, with the propagating direction θ_{n_θ} and the unit wave vector $\hat{\mathbf{k}}_{n_\theta} = \mathbf{k}_n/k_{n_\omega}$. The magnitude of the wave vector is wavenumber k_{n_ω}, which is related to the wave angular frequency ω_{n_ω} by the linear dispersion relation in deep water for conciseness in the present study. For a finite water depth, a similar equation can be easily formulated by using the fully dispersive wave number.

2.1.2. ICWM

Guérin et al. (2019) developed ICWM on the basis of Lagrangian descriptions of the ocean surface. The free surface elevation can be provided by ICWM:

$$\eta^{\mathrm{ICWM}}(x,y,t) = \sum_{n=1}^{N}\left[a_n\cos\Psi_n + b_n\sin\Psi_n + \frac{1}{2}(a_n{}^2 + b_n{}^2)k_n\right] \tag{3}$$

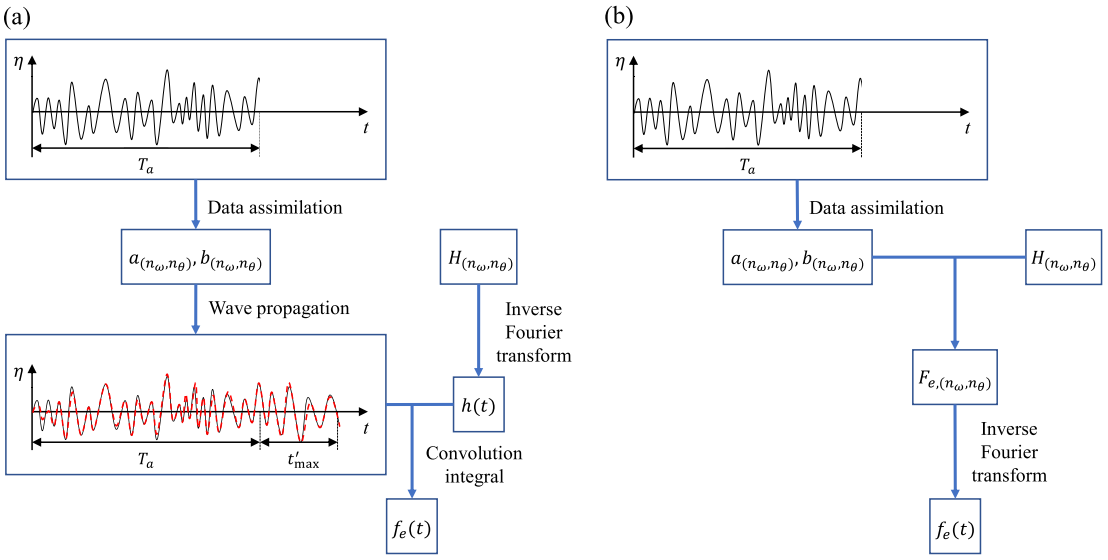

Fig. 1. Comparison of approaches for wave excitation force prediction based on (a) a convolution integral between the surface elevation $\eta(t)$ and the IRF $h(t)$, and (b) the frequency component of the excitation force $F_{e,(n_\omega,n_\theta)}$ obtained using the wave amplitude parameters $a_{(n_\omega,n_\theta)}$, $b_{(n_\omega,n_\theta)}$, and the FRF $H_{(n_\omega,n_\theta)}$ (where T_a is the assimilation time and $t_{\max} - t_r = t'_{\max}$ is the length of the practical prediction zone, with the latest time of wave reconstruction t_r and the end of prediction zone in time $t_{\max}$; ———: observed waves; - - - -: predicted waves).

where the nonlinear phase function Ψ_n includes the nonlinear wave effects such as the nonlinear phase shift, that is, the summation for particle horizontal shift in Eq. (4) and Stokes drift $\mathbf{U}_{s0}$:

$$\Psi_n = \mathbf{k}_n \cdot [\mathbf{r} - \sum_{i=1}^{N} \hat{\mathbf{k}}_i(-a_i \sin\tilde{\psi}_i + b_i \cos\tilde{\psi}_i)] - \tilde{\omega}_n t \tag{4}$$

$$\mathbf{U}_{s0} = \sum_{n=1}^{N} ({a_n}^2 + {b_n}^2)\omega_n \mathbf{k}_n \tag{5}$$

where a tilde refers to values corrected with Stokes drift, such as the corrected wave angular frequency $\tilde{\omega}_n = \omega_n + \frac{1}{2}\mathbf{k}_n \cdot \mathbf{U}_{s0}$ and the corrected nonlinear phase function $\tilde{\psi}_n = \mathbf{k}_n \cdot \mathbf{r} - \tilde{\omega}_n t$. The last term in Eq. (3) accounts for the correction with respect to the zero-mean sea level.

2.1.3. LWT-CDR

Following the recent literature on phase-resolved nonlinear wave prediction (i.e., Desmars et al., 2020; Kim et al., 2023a), we also employ linear wave theory with the corrected dispersion relation (LWT-CDR) which only involves the effect of Stokes drift. The explicit form of free surface elevation is given by LWT-CDR:

$$\eta^{\text{LWT-CDR}}(x, y, t) = \sum_{n=1}^{N} [a_n \cos\tilde{\psi}_n + b_n \sin\tilde{\psi}_n] \tag{6}$$

2.2. Data assimilation

Based on the assumption of a uniform wave field where the wave parameters (i.e., a_n and b_n) in the spatio-temporal prediction zone are unchanging, the model parameters are computed through model inversion from the measured surface elevation $\bar{\eta}$. Following previous studies (e.g., Blondel et al., 2010), we here minimize a quadratic cost function evaluating the difference between the measured surface elevation ($\bar{\eta}_l$) and the simulated one (η_l) with respect to the parameters:

$$F(\mathbf{p}) = \frac{1}{2}\sum_{l=1}^{L}[\eta_l(\mathbf{p}) - \bar{\eta}_l]^2 = \frac{1}{2}\sum_{j=1}^{J}\sum_{k=1}^{K}[\eta_{(j,k)}(\mathbf{p}) - \bar{\eta}_{(j,k)}]^2 \tag{7}$$

where $\mathbf{p} = [a_1, \ldots, a_N, b_1, \ldots, b_N]^T$ is the model coefficient vector to be obtained, and subscript l denotes the lth spatio-temporal measurement point, which is redefined in space and time $l = (j, k)$. The total number of spatio-temporal data L is a multiplication of the amount of data in space and time, J and K, respectively (i.e., $L = J \times K$).

In contrast to the simple linear assimilation, an iterative process is required because of the nonlinear phase functions employed in LWT-CDR, as well as ICWM, which are influenced by the amplitude parameters. To ensure computational stability and efficiency during the nonlinear assimilation, Kim et al. (2023a) developed simplified methods by considering the ordering system. Kim et al. (2023a) demonstrated that these new approaches are numerically straightforward and maintain model accuracy in comparison to the previous nonlinear assimilation methods. For the sake of brevity, this paper does not provide detailed explanations of the iterative process and regularization techniques for addressing challenging cases with ill-posed assimilation problems.

2.3. Excitation force prediction

Frequency-domain coefficients are commonly implemented to analyze irregular wave fields comprising a number of harmonic waves with their own amplitude, phase, and propagating direction. Specifically, the wave excitation force acting on floating structures due to incoming ocean waves can be represented using complex coefficients in the frequency domain (Cummins, 1962), such as the FRF provided by the BEM tools. The present study focuses on the real-time estimation of wave excitation force. Therefore, we assume the neglect of friction, viscous, and mooring forces, as well as nonlinear wave-structure interaction, when calculating the excitation force. Note that we account for nonlinear effects in predicting waves by employing numerically efficient nonlinear wave models; hence, the nonlinear surface waves are used as inputs for predicting force which is based on first-order wave loads.

2.3.1. First method

As presented in Fig. 1(a), when predicting the excitation force $f_e(t)$, it is typical to employ the time series of predicted surface elevation $\eta(t)$

and the IRF $h(t)$. Based on the wave amplitude coefficients obtained in the data assimilation, we compute the time-domain representation of the incident wave by evolving the free surface in space and time. Additionally, the IRF for the incident wave direction θ_e, denoted as $h_{n_{\theta_e}}(t)$, can be derived by the inverse Fourier transforms of the continuous FRF $H_{n_{\theta_e}}(\omega)$:

$$\begin{aligned} h_{n_{\theta_e}}(t) &= \frac{1}{2\pi}\int_{-\infty}^{\infty} H_{n_{\theta_e}}(\omega)\exp(-i\omega t)\,d\omega \\ &= \frac{1}{2\pi}\int_{-\infty}^{\infty} H^{*}_{n_{\theta_e}}(\omega)\exp(i\omega t)\,d\omega \end{aligned} \tag{8}$$

where the asterisk, denoting the complex conjugate, is introduced to be consistent with the convention followed in NEMOH (Babarit and Delhommeau, 2015; Kurnia and Ducrozet, 2023).

Since the actual computation is based on discrete data collection in time rather than continuous data collection, it proceeds by means of the discrete Fourier transform with the domain separated into $N_{\omega_e}\times N_{\theta_e}$ in the frequency and direction, respectively (where subscript e refers to the excitation force values). Therefore, $h_{n_{\theta_e}}(t)$ can be rewritten as the discrete formulation:

$$h_{n_{\theta_e}}(t) = \frac{1}{2N_{\omega_e}+1}\sum_{n_{\omega_e}=-N_{\omega_e}}^{N_{\omega_e}} H^{*}_{(n_{\omega_e},n_{\theta_e})}\exp\left(i\omega_{n_{\omega_e}}t\right) \tag{9}$$

where n_{ω_e} and n_{θ_e} denote the n_{ω_e}th frequency component and the n_{θ_e}th direction component of FRF. In order to keep $h_{n_{\theta_e}}(t)$ as a real-valued function, $H_{(0,n_\theta)}=0$ and $H_{(-n_{\omega_e},n_{\theta_e})}$ is defined to be the complex conjugate of $H_{(n_{\omega_e},n_{\theta_e})}$. Δf represents the frequency step of FRF and determines the n_{ω_e}th wave frequency for excitation force FRF (i.e., $\omega_{n_{\omega_e}} = 2\pi n_{\omega_e}\Delta f$).

The ocean surface elevation at the target location is decomposed into angular components propagating independently in the direction of each component:

$$\eta^{target}(t) = \sum_{n_\theta=1}^{N_\theta}\eta^{target}_{n_\theta}(t) \tag{10}$$

The IRF is interpolated into a frequency-directional discretization for the surface elevation. The excitation force can then be obtained through a convolution integral between the IRF and the predicted surface elevation at the target location:

$$f_{e,n_\theta}(t) = \int_{-\infty}^{\infty} h_{n_\theta}(\tau)\,\eta^{target}_{n_\theta}(t-\tau)\,d\tau \tag{11}$$

and

$$f_e(t) = \sum_{n_\theta=1}^{N_\theta} f_{e,n_\theta}(t) \tag{12}$$

general, the IRF is non-zero within a specific time interval (i.e., $h_{n_{\theta_e}}(\tau) \neq 0$ for $-t_c \le \tau \le t_c$), which is indicative of the non-causality of the IRF (Yu and Falnes, 1995). The half-width of the time interval with a non-zero time series (i.e., t_c) depends on the specific floating structure under investigation, which will be detailed in Section 4.3. We note that the frequency resolution Δf, required to be fine enough to accurately describe the frequency evolution of the FRF, determines the length of the IRF time series. Hence, the frequency resolution also needs to be fine enough to cover the non-zero time interval of the IRF. The upper and lower limits in the integral of Eq. (11) can thus be replaced with t_c and $-t_c$, respectively:

$$f_{e,n_\theta}(t) = \int_{-t_c}^{t_c} h_{n_\theta}(\tau)\,\eta^{target}_{n_\theta}(t-\tau)\,d\tau \tag{13}$$

When calculating the excitation force at a specific time instant t, it is necessary to have the wave information for a period t_c before and after the waves interact with the structure located on the target location (i.e., $[t-t_c, t+t_c]$, see Fig. 2).

2.3.2. Second method

It is evident that the time-domain method explained in the previous section provides estimations of wave forces. However, this approach requires performing calculations related to the wave propagation and the inverse Fourier transform, i.e. converting Fourier coefficients in the frequency domain to the function in the time domain (Eq. (9)). These are necessary because the FRF serves as a primary output of the BEM tools, and we obtain the wave amplitude parameters in the frequency domain during the first step of wave forecasting (i.e., data assimilation).

As depicted in Fig. 1(b), if the amplitude parameters $a_{(n_\omega,n_\theta)}$ and $b_{(n_\omega,n_\theta)}$, along with the FRF $H_{(n_\omega,n_\theta)}$, directly translate into the frequency components for wave force $F_{e,(n_\omega,n_\theta)}$, it can offer benefits to computational simplicity. In essence, the discrete Fourier component for surface elevation $A_{\eta,(n_\omega,n_\theta)}$ is represented by using the amplitude parameters $a_{(n_\omega,n_\theta)}$ and $b_{(n_\omega,n_\theta)}$. In a similar manner to FRF, we can decompose each of the directional components for the surface elevation into discrete frequency components:

$$\eta^{target}_{n_\theta}(t) = \frac{1}{2N_\omega+1}\sum_{n_\omega=-N_\omega}^{N_\omega} A_{\eta,(n_\omega,n_\theta)}\exp\left(i\omega_{n_\omega}t\right) \tag{14}$$

where $A_{\eta,(0,n_\theta)}=0$ is set for the zero-mean sea level.

Next, the excitation force FRF is interpolated into a frequency-directional discretization for the surface elevation to generate the frequency component for the wave excitation force, i.e. $F_{e,(n_\omega,n_\theta)}$:

$$F_{e,(n_\omega,n_\theta)} = H^{*}_{(n_\omega,n_\theta)}A_{\eta,(n_\omega,n_\theta)} \tag{15}$$

of which the summation in direction and frequency represents the excitation force:

$$f_{e,n_\theta}(t) = \frac{1}{2N_\omega+1}\sum_{n_\omega=-N_\omega}^{N_\omega} F_{e,(n_\omega,n_\theta)}\exp\left(i\omega_{n_\omega}t\right) \tag{16}$$

and

$$f_e(t) = \sum_{n_\theta=1}^{N_\theta} f_{e,n_\theta}(t) \tag{17}$$

In order to link Eq. (14) to the algorithms for wave prediction by wave models in Section 2, we manipulate Eqs. (10) and (14) by using the Euler formula:

$$\eta^{target} = \sum_{n_\theta=1}^{N_\theta}\sum_{n_\omega=1}^{N_\omega}\left[\frac{2\Re\left\{A_{\eta,(n_\omega,n_\theta)}\right\}}{2N_\omega+1}\cos\omega_{n_\omega}t - \frac{2\Im\left\{A_{\eta,(n_\omega,n_\theta)}\right\}}{2N_\omega+1}\sin\omega_{n_\omega}t\right] \tag{18}$$

where $\Re$ and $\Im$ denote the real and imaginary parts, respectively. Here, it is notable that the denominator $2N_\omega+1$ is due to the different statements of discrete Fourier transform in the frequency between the wave model and the FRF (see Eqs. (1), (2) and (9)).

The free surface elevation at the target location $\mathbf{r}_{target} = (x_{target}, y_{target})$ is given by the linear wave theory (Eq. (1)):

$$\eta^{LWT,target}(t) = \sum_{n_\theta=1}^{N_\theta}\sum_{n_\omega=1}^{N_\omega}\left[\begin{aligned} &a_{(n_\omega,n_\theta)}\cos\left(\mathbf{k}_{(n_\omega,n_\theta)}\cdot\mathbf{r}_{target}-\omega_{n_\omega}t\right) \\ &+ b_{(n_\omega,n_\theta)}\sin\left(\mathbf{k}_{(n_\omega,n_\theta)}\cdot\mathbf{r}_{target}-\omega_{n_\omega}t\right)\end{aligned}\right] \tag{19}$$

Applying the trigonometric identities and equating with Eq. (18) gives the real and imaginary parts of $A_{\eta,n}$ for LWT:

$$\begin{aligned} \Re\left\{A_{\eta,(n_\omega,n_\theta)}\right\}^{LWT} &= \frac{2N_\omega+1}{2}\left[\begin{aligned} &a_{(n_\omega,n_\theta)}\cos\left(\mathbf{k}_{(n_\omega,n_\theta)}\cdot\mathbf{r}_{target}\right) \\ &+ b_{(n_\omega,n_\theta)}\sin\left(\mathbf{k}_{(n_\omega,n_\theta)}\cdot\mathbf{r}_{target}\right)\end{aligned}\right] \\ \Im\left\{A_{\eta,(n_\omega,n_\theta)}\right\}^{LWT} &= \frac{2N_\omega+1}{2}\left[\begin{aligned} &-a_{(n_\omega,n_\theta)}\sin\left(\mathbf{k}_{(n_\omega,n_\theta)}\cdot\mathbf{r}_{target}\right) \\ &+ b_{(n_\omega,n_\theta)}\cos\left(\mathbf{k}_{(n_\omega,n_\theta)}\cdot\mathbf{r}_{target}\right)\end{aligned}\right] \end{aligned} \tag{20}$$

which are temporally invariant.

Similarly, the explicit expression of free surface elevation at the target location $\mathbf{r}_{target} = (x_{target}, y_{target})$ is provided by LWT-CDR (Eq. (6)):

$$\eta^{LWT-CDR,target}(t) = \sum_{n_\theta=1}^{N_\theta}\sum_{n_\omega=1}^{N_\omega}\left[\begin{array}{l} a_{(n_\omega,n_\theta)}\cos\left(\mathbf{k}_{(n_\omega,n_\theta)}\cdot\mathbf{r}_{target}-\tilde{\omega}_{n_\omega}t\right) \\ +\, b_{(n_\omega,n_\theta)}\sin\left(\mathbf{k}_{(n_\omega,n_\theta)}\cdot\mathbf{r}_{target}-\tilde{\omega}_{n_\omega}t\right)\end{array}\right] \tag{21}$$

Separating the corrected wave angular frequency into the contribution of Stokes drift and the linear wave angular frequency:

$$\eta^{LWT-CDR,target}(t) = \sum_{n_\theta=1}^{N_\theta}\sum_{n_\omega=1}^{N_\omega}\left[\begin{array}{l} a_{(n_\omega,n_\theta)}\cos\left(\mathbf{k}_{(n_\omega,n_\theta)}\cdot\mathbf{r}_{target}-\frac{1}{2}\mathbf{k}_{(n_\omega,n_\theta)}\cdot\mathbf{U}_{s0}t-\omega_{n_\omega}t\right) \\ +\, b_{(n_\omega,n_\theta)}\sin\left(\mathbf{k}_{(n_\omega,n_\theta)}\cdot\mathbf{r}_{target}-\frac{1}{2}\mathbf{k}_{(n_\omega,n_\theta)}\cdot\mathbf{U}_{s0}t-\omega_{n_\omega}t\right)\end{array}\right] \tag{22}$$

Again, we use the trigonometric identities, and equating with Eq. (18) leads to

$$\begin{aligned}&\Re\left\{A_{\eta,(n_\omega,n_\theta)}\right\}^{LWT-CDR} \\ &= \frac{2N_\omega+1}{2}\left[\begin{array}{l} a_{(n_\omega,n_\theta)}\cos\left(\mathbf{k}_{(n_\omega,n_\theta)}\cdot\left[\mathbf{r}_{target}-\frac{1}{2}\mathbf{U}_{s0}t\right]\right) \\ +\, b_{(n_\omega,n_\theta)}\sin\left(\mathbf{k}_{(n_\omega,n_\theta)}\cdot\left[\mathbf{r}_{target}-\frac{1}{2}\mathbf{U}_{s0}t\right]\right)\end{array}\right] \\ &\Im\left\{A_{\eta,(n_\omega,n_\theta)}\right\}^{LWT-CDR} \\ &= \frac{2N_\omega+1}{2}\left[\begin{array}{l} -\,a_{(n_\omega,n_\theta)}\sin\left(\mathbf{k}_{(n_\omega,n_\theta)}\cdot\left[\mathbf{r}_{target}-\frac{1}{2}\mathbf{U}_{s0}t\right]\right) \\ +\, b_{(n_\omega,n_\theta)}\cos\left(\mathbf{k}_{(n_\omega,n_\theta)}\cdot\left[\mathbf{r}_{target}-\frac{1}{2}\mathbf{U}_{s0}t\right]\right)\end{array}\right]\end{aligned} \tag{23}$$

Compared to the formulations given by LWT in Eq. (20), the formulations provided by LWT-CDR, i.e. Eq. (23) are time-dependent functions. It is desirable to see the change in time traveled as it reflects the phase shift induced by the Stokes drift. In this way, the nonlinear wave model is able to be implemented alongside the linearized system of force calculation in the second method. Due to the correction with respect to the nonlinear phase aspect, which is essential for wave prediction algorithms, the resulting force calculation is partly nonlinear.

Lastly, to the best of the authors' knowledge, the Fourier expression for the surface elevation by ICWM is non-derivable due to the terms introduced for the zero-mean sea surface in Eq. (3). Nonetheless, the wave force estimation based on wave prediction by ICWM can still be obtained using the time-domain method.

2.4. Prediction zone

When we provide a phase-resolved wave forecast based on the finite measured wave field, it is essential to define the relevant prediction zone in time and space. This zone represents the spatio-temporal region where the initial conditions derived from the wave measurements can properly explain the future behavior of the ocean surface. The accuracy of the wave excitation force relies on the deterministic wave forecast; therefore, the force prediction zone is closely dependent on the wave prediction zone.

In Fig. 2, the wave prediction zone in time ($t' \in [t'_{\min}, t'_{\max}]$ where $t' = t - t_r$ with t_r being the latest time of wave reconstruction) is composed of times for nowcast and forecast, indicated by the red shading and the gray shading, respectively. The temporal wave prediction zone is established by the assimilation time T_a, the distance between observation points and the target point, and the simulated wave field. Compared to the temporal prediction zone for waves, the one for excitation force has the potential to change. This is due to the inclusion of the wave surface elevation interval over $[t - t_c, t + t_c]$ when computing the force at a specific time instant t. Specifically, when predicting the wave force at the boundaries of the prediction zone (i.e., $t' = t'_{\min}$ or $t'_{\max}$), half of the wave estimation interval extends beyond the prediction zone. In contrast, the force estimation for the midpoint of the wave prediction zone is on the basis of all the predicted waves within the prediction zone. Therefore, the theoretical prediction zone for excitation forces is expected to be reduced at both ends by t_c, i.e. $[t'_{e,\min}, t'_{e,\max}] = [t'_{\min} + t_c, t'_{\max} - t_c]$.

It is noteworthy that the two methods suggested in Section 2.3 are interchangeable, and the objective of the second method is developed to simplify calculations. Thus, not only the non-causality but also the possible change in the force prediction zone in time, relative to the wave prediction in time, is relevant irrespective of the chosen approach for force estimation.

Table 1
Wave information and setup of experiments.

Case	H_s (m)	H_s/L_p (%)	s	J_θ	N_θ
M1	5	2.2	25	9	9
M2	7	3.1	25	9	7
M3	9	4.0	25	9	7
M4	7	3.1	15	11	9
M5	7	3.1	60	7	5
U1	5	2.2	∞	1	1
U2	7	3.1	∞	1	1
U3	9	4.0	∞	1	1

3. Experimental data

During the campaigns of the FLOATECH project, experiments were conducted in the hydrodynamic and ocean engineering tank at École Centrale de Nantes (ECN) (Bonnefoy et al., 2023). The tank is 30 m wide, 50 m long, and 5 m deep, with a wavemaker at one end, composed of 48 individual hinged flaps, and a stainless steel beach at the other end. The wave tank tests were conducted under irregular sea states using a Pierson–Moskowitz spectrum (Pierson and Moskowitz, 1964) with a peak period $T_p = 12$ s at full scale and at the geometric scale of 1:40 (1: $\sqrt{40}$ Froude scaling for time).

3.1. Wave tests

The wave tests were conducted to examine the propagation of ocean surface waves toward the target location. Table 1 shows the experimental wave information and setup for all the cases. The significant wave heights were selected to vary the characteristic wave steepness from $H_s/L_p = 2.2\%$ to $H_s/L_p = 4\%$ in deep water ($k_p d \approx 5.6$), with a peak wavelength $L_p = 225$ m (5.62 m at tank scale). For completeness, the sea states with different directional spreads were also considered (see Fig. 3). Different directional spreads in the wave field were taken into account by an angular spreading function in (Mitsuyasu et al., 1975):

$$G(\theta) = \frac{2^{2s-1}}{180}\frac{(s!)^2}{(2s)!}\cos^{2s}\left(\frac{\theta}{2}\right) \text{ for } \theta \in [-180°, 180°] \tag{24}$$

where θ is the propagating direction, s is the directional spreading factor, and the average direction of propagation is 0°. In addition to the multidirectional cases, we investigate the unidirectional cases with the same range of H_s where $s = \infty$ denotes the long-crested waves in Table 1.

To replicate a situation with a structure-mounted remote sensor, a matrix of $J_r \times J_\theta$ rays in the xy-plane was made by utilizing the 20 wave gauges installed on a straight rotating structure (i.e., $J_r = 20$, see Fig. 4). The actual changes in the location of the wave gauges resulting from the intersections between active rays pointing from an optical sensor and a dynamic ocean surface (or shadowing effects) were not taken into consideration. We located four additional downstream wave gauges including WG21 (or target location), WG22, WG23, and WG24 to which the propagating distances from the region of measurements are about

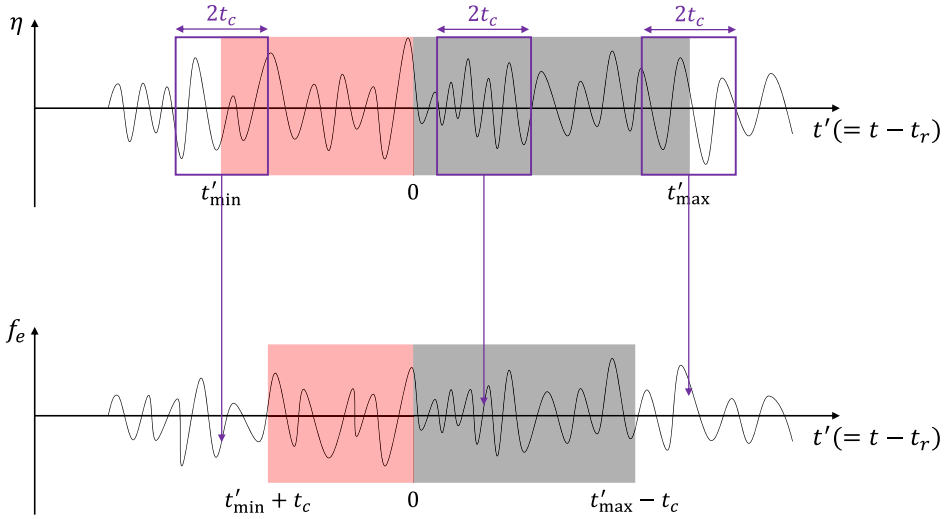

Fig. 2. Prediction zones in time for wave and force where purple rectangles encompass wave surface elevation interval when computing forces (red shading: nowcast; gray shading: forecast).

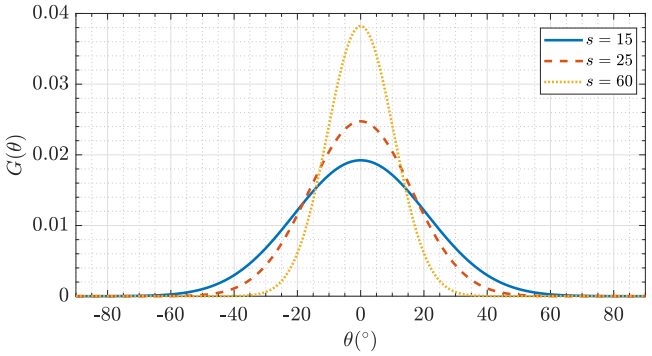

Fig. 3. Directional spreading for multidirectional cases where s is the directional spreading factor (———: $s = 15$; − − − −: $s = 25$; ·····: $s = 60$).

$0.15L_p$, $0.21L_p$, $0.24L_p$, and $0.28L_p$, respectively. At $t_a/T_p \approx 158$, all the wave components generated by the wavemaker can be considered to have reached the experimental domain. We used the time series up to the end of the time series measured in experiments, where $t_b/T_p \approx 664$ and $t_b - t_a \approx 506T_p$, because wave surface elevation was measured until the wavemaker was turned off. For the detailed experimental setup (e.g., a sketch of an optical system), the reader is referred to Kim et al. (2023a).

3.2. Excitation force tests

To evaluate the estimation of excitation forces based on deterministic sea wave prediction, we conducted additional tests to measure the wave excitation forces at the center of the platform model on the free surface. A set of load vectors, including three forces and three moments in the x, y, and z coordinate system, was collected by a 6-component load cell installed on top of a platform model.

A tripod was installed in the wave tank, carrying an inverted hexapod used to maintain a fixed position of the model. The platform model (scale 1:40), was positioned below the hexapod with a rigid connection by means of a stiff load cell located at the junction between the platform model and the hexapod. The hexapod was held in a fixed position, as was the model (see Fig. 5). The same sea states as those used in the wave tests are reproduced. The experiments were not conducted for wave conditions with $H_s = 9$ m due to the limited capacity of the load cell with respect to the second moment component (i.e., M_y).

Table 2
Geometry and mass of platform model (full scale).

Item	Value
Draft (m)	90
Diameter below tapper (m)	18
Diameter at waterline (m)	11.2
Top of the tapper w.r.t. waterline (m)	4
Distance between the load cell and waterline (m)	7.24
Length of tapper (m)	8
Platform height above waterline (m)	4
Platform mass (kg)	1.92E+07
Platform COG w.r.t. waterline (m)	−70.92
Platform pitch inertia at COG (kg m^2)	1.05E+10

Geometry and mass properties of the platform model are given at full scale in Table 2 (Leroy et al., 2022). The first bending mode of the model has a frequency of 1.82 Hz at a 1:40 model scale. This frequency is large enough to avoid disturbances in the wave frequencies of interest. The load cell has a high nominal measurement for the vertical force, resulting in significant uncertainty in the measurement of the F_z component (about 5% of the measured loads). For the other components (i.e., F_x and M_y), the relative uncertainties are very low, with estimated values of respectively 0.6% and 0.05%.

The excitation forces measured by locking the floating structure in a fixed position are approximate values as the structure's location is variable in the presence of the wave field (Hillis et al., 2020). However, from the modeling point of view, the linearized system can be developed based on the same location, which is consistent with the first-order wave loads from NEMOH. Note that we performed other experiments with the floating structure placed freely, which are not presented here. In those experiments, we observed surge motions with a typical amplitude of 10 m (full scale) in response to waves with an amplitude of 3 m, a period of 12 s, and a platform diameter of 18 m. This result is compatible with the use of linear theory.

4. Numerical results

To evaluate the model performance for surface elevation and wave excitation force, we synthesize an ensemble using partly overlapping

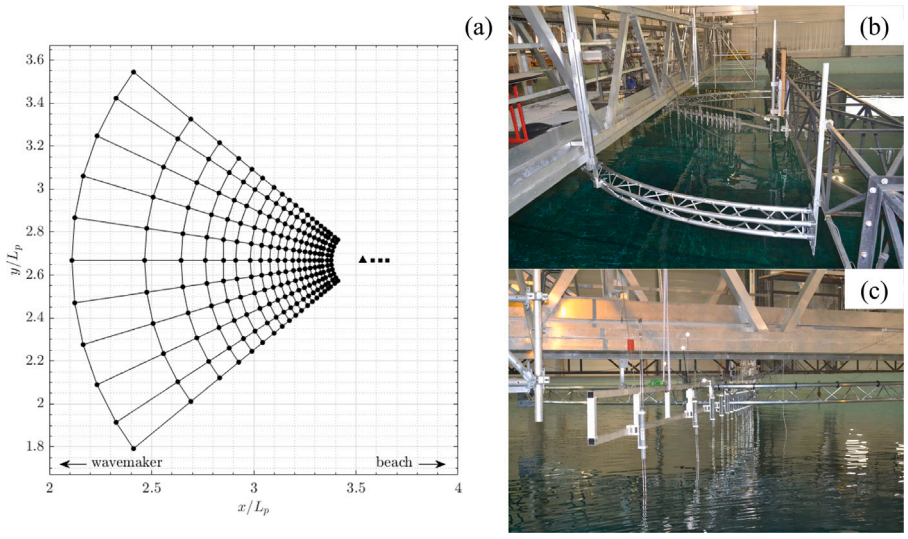

Fig. 4. (a) Location of wave gauges; (b, c) wave gauges mounted on rotating structure (•: wave observations; ▲: location of turbine, WG21; ■: three additional downstream WG22, WG23, and WG24).

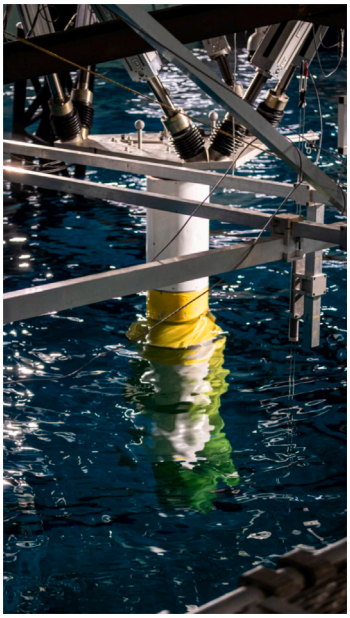

Fig. 5. Installation of captive platform model, where the rigid connection between the model platform in yellow and the hexapod (not visible here).

surface samples with a shifting time Δt. A large number of surface samples, each consisting of one nowcast (or assimilation) and one forecast (or prediction), were generated based on a single sea state over a sufficiently long period. These samples were then used to measure misfit errors:

$$\varepsilon_\eta(x,y,t) = \frac{1}{N_s}\sum_{i=1}^{N_s}\frac{\left|\eta_{pred,i}(x,y,t) - \eta_{ref,i}(x,y,t)\right|}{4\sigma_\eta}$$
$$\varepsilon_{f_e}(x,y,t) = \frac{1}{N_s}\sum_{i=1}^{N_s}\frac{\left|f_{e,pred,i}(x,y,t) - f_{e,ref,i}(x,y,t)\right|}{4\sigma_{f_e}} \quad (25)$$

where subscripts $pred, i$ and ref, i refer to the prediction and reference values of surface elevation or excitation force from the ith surface sample, respectively, and σ denotes the standard deviation of the reference values. The misfit errors are further averaged in time across the time prediction zone $[t_{\min}, t_{\max}]$:

$$\varepsilon_\eta^p(x,y) = \frac{1}{t_{\max}-t_{\min}}\int_{t_{\min}}^{t_{\max}}\varepsilon_\eta(x,y,t)\,dt$$
$$\varepsilon_{f_e}^p(x,y) = \frac{1}{t_{\max}-t_{\min}}\int_{t_{\min}}^{t_{\max}}\varepsilon_{f_e}(x,y,t)\,dt \quad (26)$$

Following Kim et al. (2023a), we used $N_s = 400$ with $\Delta t/T_p = 0.053$ to calculate the misfit error, which yielded accurate results with fast convergence.

The surface similarity parameter (SSP), suggested by Perlin and Bustamante (2016), is likely to assess an over-predicted value higher than an under-predicted one. Accordingly, Kim et al. (2023a) proposed the improved surface similarity parameter (ISSP) based on the deviation from the frequency-averaged reference value $\overline{F}_{\eta,ref}$. In addition to the misfit error, we quantify the model accuracy by calculating the ISSP values throughout the whole experimental duration up to t_b (where $t_b - t_a \approx 506T_p$) in all cases:

$$ISSP_\eta = \frac{\left(\int\left|F_{\eta,pred}(f) - F_{\eta,ref}(f)\right|^2 df\right)^{1/2}}{\left(\int\left[\left|F_{\eta,pred}(f) - \overline{F}_{\eta,ref}\right| + \left|F_{\eta,ref}(f) - \overline{F}_{\eta,ref}\right|\right]^2 df\right)^{1/2}}$$
$$ISSP_{f_e} = \frac{\left(\int\left|F_{f_e,pred}(f) - F_{f_e,ref}(f)\right|^2 df\right)^{1/2}}{\left(\int\left[\left|F_{f_e,pred}(f) - \overline{F}_{f_e,ref}\right| + \left|F_{f_e,ref}(f) - \overline{F}_{f_e,ref}\right|\right]^2 df\right)^{1/2}} \quad (27)$$

where $F_{\eta,pred}$, $F_{f_e,pred}$ and $F_{\eta,ref}$, $F_{f_e,ref}$ are Fourier coefficients of wave and force time series for prediction and reference values, respectively. Note that the entire experimental duration was split into the surface samples with a shifting time Δt, and the first point of the forecast waves at each sample was collected to extract the spectral density.

4.1. Wave parameters for prediction

The wave information used in the data assimilation is critical in estimating the future sea state. The same wave parameters were employed in this study as those used in Kim et al. (2023a). For the spatio-temporal wave measurements, the number of data in time K (or assimilation time $T_a = (K-1)\Delta t$) greatly influences both model performance and computational cost of the nonlinear models, while the number of data

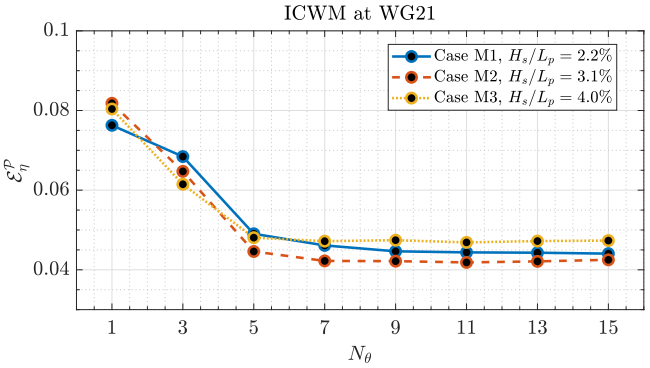

Fig. 6. Misfit error of surface elevation by ICWM at WG21 against N_θ (———: Case M1; – – – –: Case M2; ·····: Case M3).

in space was given (i.e., $J = J_r \times J_\theta = 20 \times J_\theta$, see Table 1). We applied $K = 100$ (or $T_a/T_p \approx 5.2$), which was determined to yield the error convergence; a further increase in K did not make any difference in model accuracy.

The model-based predictions from the wave observations also rely on the bandwidths in frequency and direction from a numerical point of view. he minimum wavenumber in the finite wavenumber bandwidth k_1, related to the largest measurable wavelength in given experimental and numerical setups, is provided by the distance in the x-direction between the beginning and end of the wave gauges for each case (x_b and x_e), along with the assimilation time T_a:

$$k_1 = \frac{2\pi}{x_e - x_b + c_{g,N_\omega} T_a} \tag{28}$$

where the N_ωth wavenumber k_{N_ω} relates to the slowest group velocity c_{g,N_ω} by the deep water linear dispersion relation. Hence, the last frequency component's wavenumber k_{N_ω} is necessarily prespecified and corresponds to the upper limit of the frequency bandwidth. We applied $k_{N_\omega} = 12k_p$ with $N_\omega = 30$, which ensures a good balance between the model accuracy and the numerical efficiency. Kim et al. (2023b) optimized N_ω with considering the same linear relationship between k_{N_ω} and N_ω as in Desmars et al. (2020).

The cutoff limits in the wave direction $[\theta_{\min} = -45°, \theta_{\max} = 45°]$, where $\theta_{\min}$ and $\theta_{\max}$ are the minimum and maximum wave directions, respectively, are chosen, such that the remainder of spectral density is negligible outside the directional limits. For a practical implementation at a real sea state, it may be necessary to select a narrower direction bandwidth, considering that the optimal system has a finite limit on the range of arriving directions at the floating structures. Moreover, depending on the desired target accuracy or the directional FRF of interest, it is preferable to use different conditions (e.g., narrower direction bandwidths or fewer wave components in direction).

Kim et al. (2023a) optimized N_θ in the multidirectional cases with the same wave steepness of 3.1% but different directional spreads (i.e., Cases M2, M4, and M5, see Table 1). Given that a greater N_θ results in increased computational costs, the optimal value of N_θ is the one that leads to error convergence. It is evident that the optimal N_θ increases with greater direction spreading.

In this study, we determined the best value of N_θ in the multidirectional cases with varying wave steepnesses (i.e., Cases M1, M2, M3, see Fig. 6). We obtained an optimal N_θ value of 9 in Case M1 with the smallest wave steepness, while $N_\theta = 7$ was found to be optimal for Cases M2 and M3. In addition, the reduction in the misfit error with the increasing N_θ around $N_\theta = 7$ was found to be more evident in Case M2 compared to Case M3. These optimized values of N_θ with varying wave steepness, combined with those with different directional spreads in Kim et al. (2023a), conclude that the optimal N_θ increases with decreasing wave steepness and increasing directional spreading. A similar conclusion was made by Babanin et al. (2010), indicating that a strong nonlinearity can counteract the focusing impact of directionality in terms of the driving force behind nonlinear wave evolution.

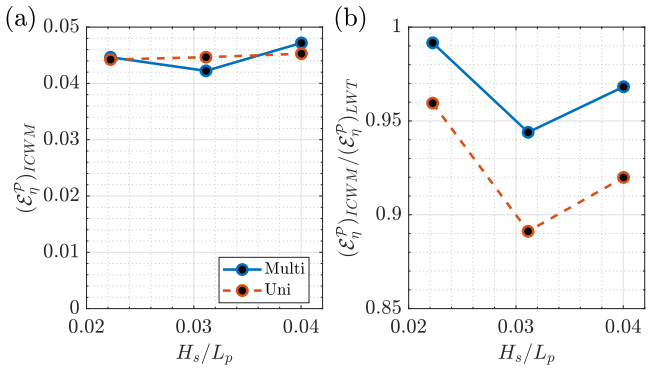

Fig. 7. (a) Prediction errors ϵ_η^p of surface elevation by ICWM at WG21; (b) Comparison of prediction errors ϵ_η^p of surface elevation between ICWM and LWT at WG21 (———: multidirectional cases; – – – –: unidirectional cases).

4.2. Overview of wave prediction performance

This section demonstrates that the predicted waves show excellent agreement with the measurements, regardless of wave steepness and directional spreading, in both multidirectional and unidirectional seas. Fig. 7(a) presents the wave prediction errors by ICWM with increasing wave steepness for both unidirectional and multidirectional cases. It was found that the directional spreading has little or no impact on the prediction accuracy (Kim et al., 2023a; not shown here for the sake of conciseness). Thus, the wave prediction algorithms based on ICWM are validated with high precision in all experimental configurations with a significantly low misfit error of about 4.5%. Time series comparison will be provided in later sections (i.e., Figs 11(a) and 17(a)).

The effect of wave steepness on surface elevation prediction is illustrated by analyzing both multidirectional and unidirectional cases with the same directional spreading but different wave steepnesses H_s/L_p. The wave steepness is unlikely to have a significant effect on the model accuracy of ICWM. This result is expected due to the experimental noise. Desmars et al. (2020) compared the experimental and numerical surface elevation data to the simulated results in an equivalent experimental setup, albeit with a somewhat shorter peak period ($T_p = 10$ s). The authors confirmed, through a "noisy numerical data set" generated by including a noise signal into the numerical data, that it is the experimental noise that contributes to the higher experimental prediction error than the theoretical one. In addition, this limited impact of the wave steepness may be associated with the fact that ICWM partly takes into account nonlinear aspects.

Fig. 7(b) presents a comparison between ICWM and LWT as the wave steepness increases in both multidirectional and unidirectional cases. By comparing the prediction errors of surface elevation between

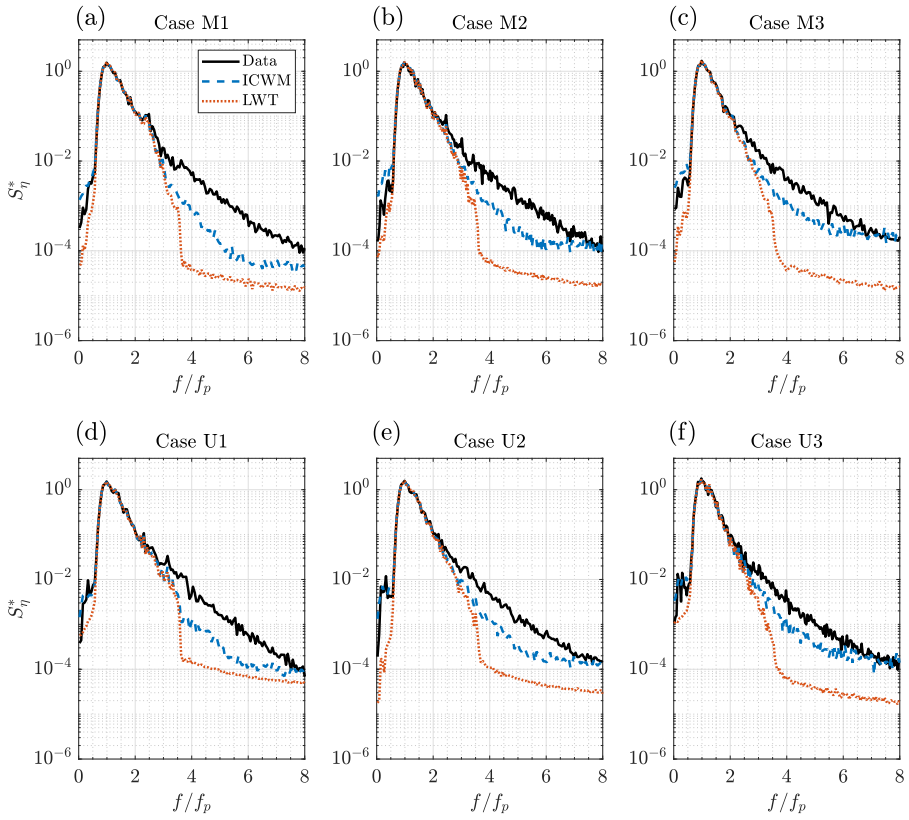

Fig. 8. Normalized wave spectra of surface elevation at WG21: (a) Case M1; (b) Case M2; (c) Case M3; (d) Case U1; (e) Case U2; (f) Case U3 (———: Data; – – – –: ICWM; ·····: LWT).

ICWM and LWT, it appears that wave nonlinearity has a relatively significant effect on the evolution of sea states. When the wave steepness increases from 2.2% to 3.1% (from Cases M1 and U1 to Cases M2 and U2, respectively), the error ratio of ICWM to LWT decreases. With a further increase in H_s/L_p (from Cases M2 and U2 to Cases M3 and U3, respectively), the ratio moves in the opposite direction. This result in Cases M3 and U3 aligns with the findings in Desmars et al. (2020) for a case with $H_s/L_p = 4.48\%$. The abnormal behavior was likely attributed to strong wave-breaking because the breaking mechanism was neglected in the wave simulation, and thus only the observed spectra were influenced by wave breaking. We also observed strong wave-breaking and the simulated waves by ICWM being closer to LWT in Cases M3 and U3 in this study.

Fig. 8 compares the normalized wave spectra $S_\eta^* = S_\eta f_p/(H_s^2/16)$, extracted from the time series for the entire experimental duration at WG21. In Cases M3 and U3, the experimental spectra in the high-frequency range are located between those of LWT and ICWM, namely, ICWM slightly overestimates the high-frequency components. It is worth noting that wave-breaking-induced energy dissipation increases with the square of frequency (Mase and Kirby, 1992; Chen et al., 1997). The intensity of frequency dependence for dissipation increases with wave height, despite its weak intensity in deep water (Kim and Kaihatu, 2022). On the other hand, the greater errors of LWT are mainly due to its inadequate representation of high-frequency wave spectra ($f/f_p > 3.5$), while ICWM shows better performance in capturing the evolution of wave spectral density across the high-frequency range (Desmars et al., 2020; Kim et al., 2023a). In summary, when wave breaking becomes dominant over the nonlinear wave effects, as in Cases M3 and U3, the differences between the results of ICWM and LWT become less evident.

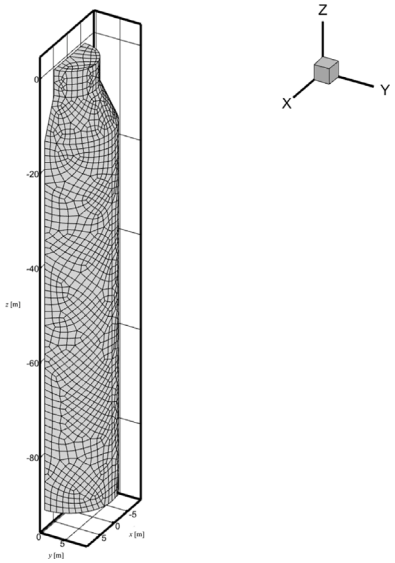

Fig. 9. Panel mesh of floating platform structure.

4.3. Excitation force prediction

Based on the open-source BEM software NEMOH (Babarit and Delhommeau, 2015; Kurnia and Ducrozet, 2023), the excitation forces exerted on the floating body of interest are represented. The first-order

wave loads on the floating platform structure are studied based on a mesh with 1872 panels as shown in Fig. 9. The mesh was carefully chosen after a proper convergence study. Since the geometry of the structure is axisymmetric with a circular cross-section floating on the ocean surface and the wave field is confined to the propagation at limited angles with the x-axis, the motion of the body mainly occurs in the surge force F_x, the heave force F_z, and the pitch moment M_y degrees of freedom (DOFs).

Fig. 10 illustrates the magnitude and phase of the complex frequency response function and corresponding impulse response function in the time domain for the three DOFs at full scale. The frequency and direction intervals selected for the boundary element solver are $\omega_e \in [0.02\pi \text{ rad/s}, 2\pi \text{ rad/s}]$ with $N_{\omega_e} = 200$ and $\theta_e \in [-90°, 90°]$ with $N_{\theta_e} = 11$, respectively. Due to the geometry of the structure, the values of FRF and IRF within the prespecified directional bandwidth $[\theta_{\min} = -45°, \theta_{\max} = 45°]$ vary slightly with the propagating direction of the incoming wave. The FRF and IRF remain the same in the direction of the wave, varying only in the reference frame used for the calculation, in which the waves are rotated. Also, for the negative angle of propagation (i.e., $-\theta$), the assigned response functions are entirely equivalent to those for θ. The non-causality is easily recognized in the IRF for the excitation forces in all three DOFs from Fig. 10(b), (d), and (f) where part of positive impulse (i.e., $h(\tau) \neq 0$ for $\tau < 0$) is as large as part of negative impulse (i.e., $h(\tau) \neq 0$ for $\tau > 0$). The half-width of the time interval with non-zero IRF (i.e., t_c) is about 12 s at the greatest.

4.3.1. Force prediction for unidirectional waves

Several authors have derived theoretical wave excitation forces by performing convolution integrals between the IRF from BEM packages and the measured surface elevation at the structure location. They then compared the theoretical values with numerical results (e.g., Guo et al., 2017, 2018; Hillis et al., 2020). In this section, the wave force estimations are validated by comparing the predicted excitation forces $f_{e,pred}(t)$ ($\eta_{pred} * h(t)$ or using a_n, b_n, and H_n) with the theoretical ones $\eta_{ref} * h(t)$ and the experimental ones $f_{e,ref}(t)$. The solid lines in Figs. 11 and 14 indicate the experimental waves $\eta_{ref}(t)$ and the theoretical forces $f_{e,ref}(t)$, respectively. For compactness of presentation, we present detailed results only for one unidirectional wave case with moderate wave steepness (i.e., Case U2). In the unidirectional cases, we also compute several quantities between the predictive and theoretical wave forces in order to analyze the effect of the IRF on the results, specifically focusing on the differences between force components and between waves and forces.

Fig. 11 presents the time series of the surface elevation and excitation forces, where the values are normalized by their own standard deviations. The comparison of model prediction by ICWM to the experimental results shows reasonable agreement in the wave force prediction for all components, with occasional discrepancies in some wave crests and troughs primarily attributed to the first-order wave loads from NEMOH. However, we identified no or little effect of the wave steepness on the deviations from the measured time series under the considered wave conditions for the force tests (i.e., between Cases U1 and U2, which is also shown in Fig. 12). Besides, the deviation of the F_z can be attributed to the instrument's measurement uncertainty on the F_z compared to the other components. Due to this limitation, a smoothing window with a span of about $0.1T_p$ was applied to reduce the noise in Fig. 11. In the context of the feed-forward controller of floating offshore wind turbines, the surge force (F_x) and the pitch moment (M_z) are more critical than the heave force (F_z) (Al et al., 2020).

It is clear that the numerical results show a better match with the theoretical values for the excitation forces compared to the surface elevation. This higher prediction accuracy for the force is consistent with the comparison of prediction errors of ICWM in Figs. 12(a) and 13(a). These results are unsurprising, as the magnitude of FRF $|H_n|$ acts as a frequency-weighting factor toward the low-frequency range, thereby reducing the relatively high deviation of all the models from the reference data across the high-frequency range.

As shown in Figs. 12(b), (c) and 13(b), (c), ICWM provides a better estimation for the F_x component of excitation forces compared to LWT and LWT-CDR. Contrary to the F_x component, every model appears to provide almost the same results for the other components. These findings are owing to the fact that the force computation for the F_z and M_y components involves fewer wave components in the high-frequency range. Consequently, the differences between the predictive

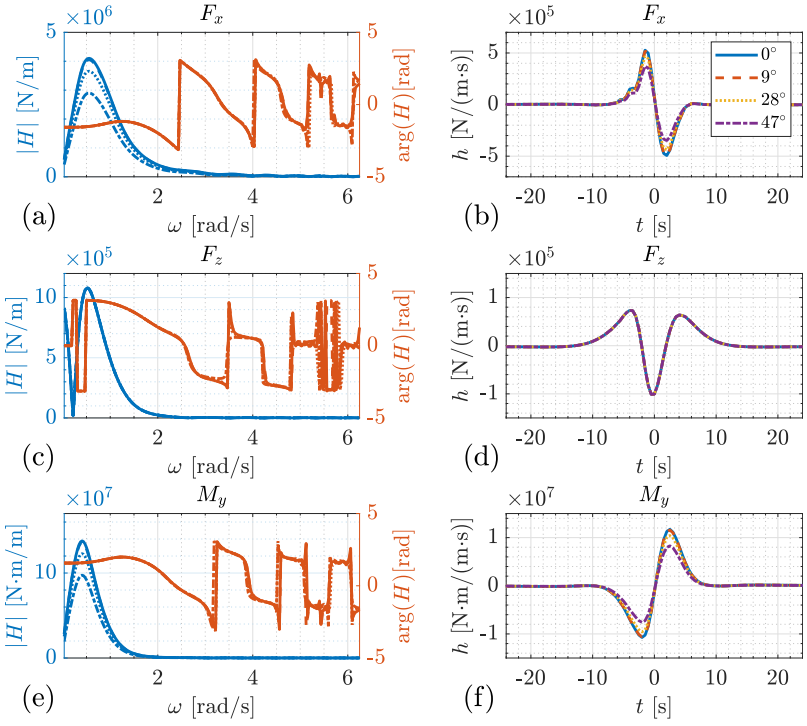

Fig. 10. Magnitude and phase of FRF and corresponding IRF from NEMOH: (a) FRF of surge; (b) IRF of surge; (c) FRF of heave; (d) IRF of heave (e) FRF of pitch; (f) IRF of pitch (———: 0°; – – – –: 9°; ·····: 28°; —·—: 47°).

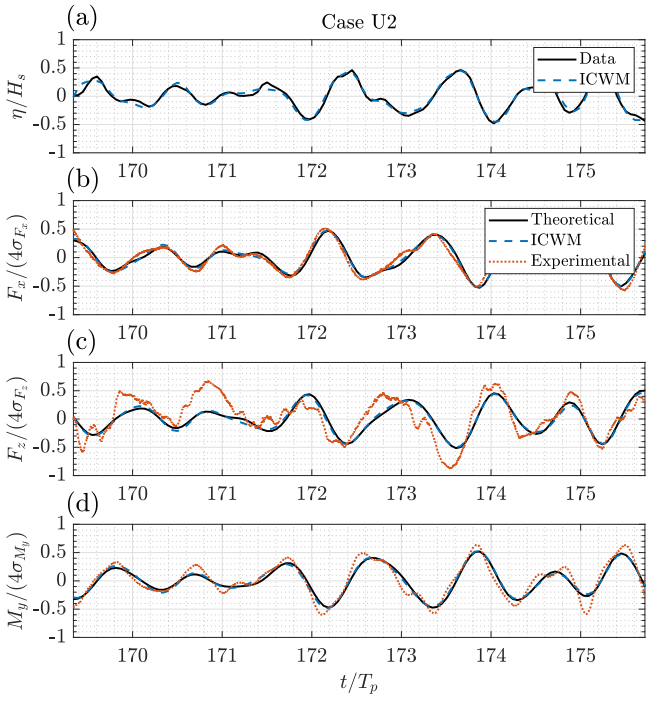

Fig. 11. Time series of surface elevation and excitation force for Case U2 at WG21: (a) η; (b) F_x; (c) F_z; (d) M_y (———: experimental waves $\eta_{ref}(t)$ in panel (a) and theoretical forces $\eta_{ref} * h(t)$ in panels (b), (c), and (d); – – – –: ICWM $f_{e,pred}(t)$ ($\eta_{pred} * h(t)$); ·····: experimental forces $f_{e,ref}(t)$).

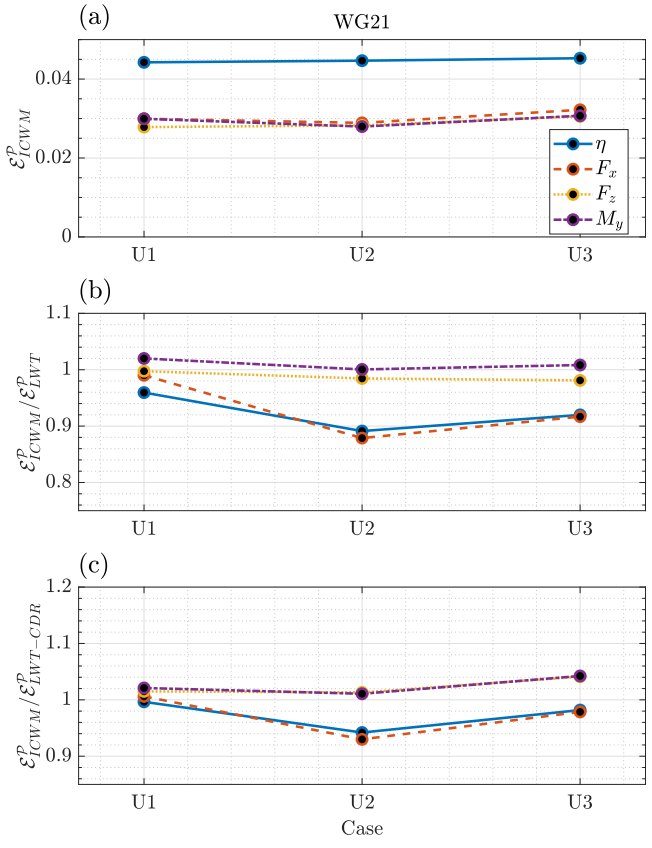

Fig. 12. Comparison of misfit error between surface elevation and excitation forces for unidirectional cases at WG21: (a) error by ICWM; (b) ratio of ICWM to LWT; (c) ratio of ICWM to LWT-CDR (———: η; – – – –: F_x; ·····: F_z; —·—: M_y).

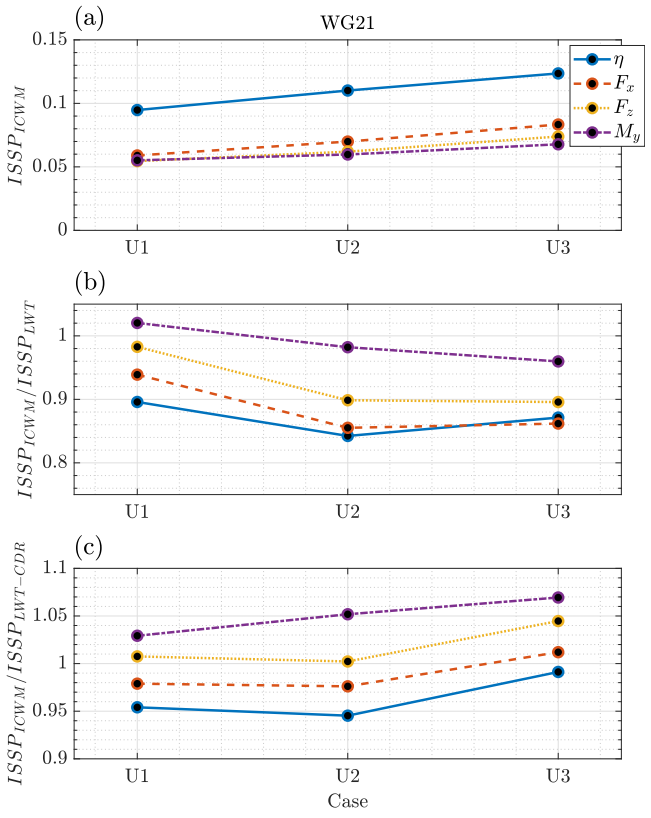

Fig. 13. Comparison of ISSP between surface elevation and excitation forces for unidirectional cases at WG21: (a) error by ICWM; (b) ratio of ICWM to LWT; (c) ratio of ICWM to LWT-CDR (———: η; – – – –: F_x; ·····: F_z; —·—: M_y).

and theoretical values, as well as between the results of nonlinear and linear models, become less significant.

The comparison of wave spectra for both the waves and forces in Fig. 14 shows that the differences in the high-frequency range become negligible for the excitation force. It should be noted that the nearly zero value at the high-frequency range may have minimal contributions to the description of excitation force, despite the high-frequency spectra being overestimated by ICWM. The natural frequency of the structure accounts for the generation of secondary peaks in the measured excitation force spectra. The abnormal deviation in the spectral descriptions for the F_z component also results from the measurement uncertainty of the instrument.

4.3.2. Force prediction zone

Section 2.4 describes possible modifications to the prediction zone in time for wave force prediction because prediction errors near the boundaries of the prediction zone (i.e, $t'_{\min}$ and $t'_{\max}$) may exceed the tolerable level. According to Kim et al. (2023a), in the unidirectional case of their experimental campaign, the practical zone in time for wave prediction was determined as $t' \in [t'_{\min}, t'_{\max}] = [-4.5T_p, 1.9T_p]$, where T_p is the peak period. Therefore, the theoretical prediction zone for excitation forces is expected to be reduced at both ends by t_c, i.e. $[t'_{e,\min}, t'_{e,\max}] = [-4.5T_p + t_c, 1.9T_p - t_c]$. The temporal evolution of misfit errors by ICWM for Case U2 at WG21 is illustrated in Fig. 15, where solid-o lines represent the boundaries of the wave prediction zone, i.e. $[t'_{\min}, t'_{\max}] = [-4.5T_p, 1.9T_p]$. The force prediction zone, indicated by dotted-x lines, corresponds to the case with $t_c = 12$ s. However, this approach appears to be safer for all the excitation forces.

We employ the wave information during the time interval t_c before and after the waves impact the floating structure at t (i.e., $[t - t_c, t + t_c]$, see Fig. 2) to calculate excitation force in both the frequency- and

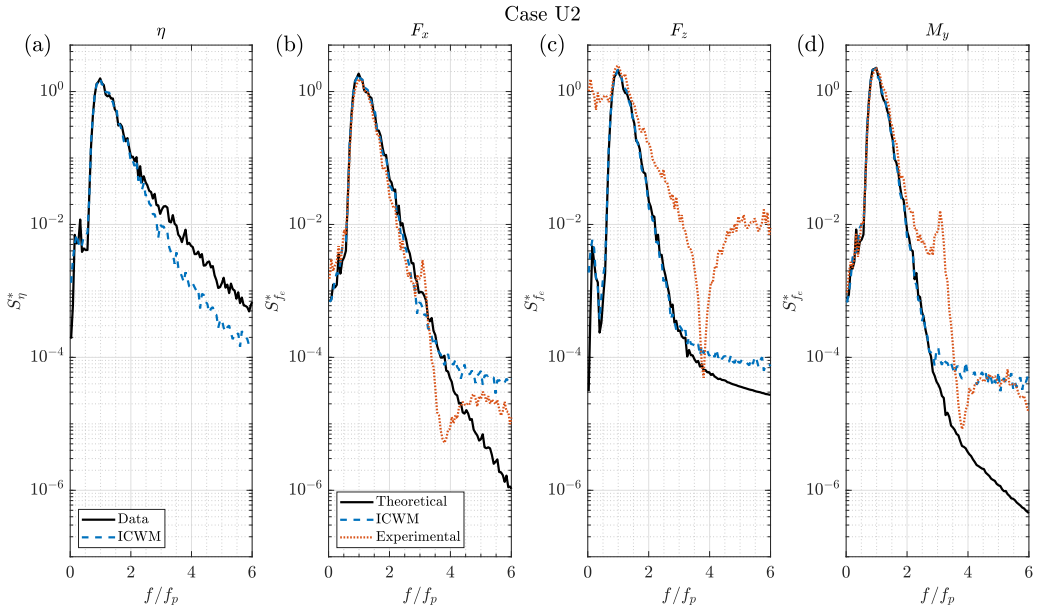

Fig. 14. Normalized wave spectra of surface elevation and excitation force for Case U2 at WG21: (a) η; (b) F_x; (c) F_z; (d) M_y (———: experimental waves $\eta_{ref}(t)$ in panel (a) and theoretical forces $\eta_{ref} * h(t)$ in panels (b), (c), and (d); – – – –: ICWM $f_{e,pred}(t)$ (or $\eta_{pred} * h(t)$); ·····: experimental forces $f_{e,ref}(t)$).

time-domains. Therefore, when one estimates the excitation force at the boundaries of the wave prediction zone (e.g., $t'_{\max}$), half of the wave forecast falls outside the prediction zone (e.g., $[t'_{\max}, t'_{\max} + t_c]$). This leads to a sharp increase in prediction error for the excitation forces at the boundaries of the wave prediction zone, as shown in Fig. 15. However, the other half (e.g., $[t'_{\max} - t_c, t'_{\max}]$) is inside the wave prediction zone, and thus errors for the excitation forces remain very small over the wave prediction zone. As a result, the same prediction zone can be applied to the excitation forces as to the surface elevations (i.e., $[t'_{e,\min}, t'_{e,\max}] = [-4.5T_p, 1.9T_p]$).

The behavior of the FRF as the frequency-weighting factor toward the low-frequency range (i.e., $\omega \approx 0.5$ rad/s), resulting in the narrower force spectrum, can help explain why the same prediction zone is applicable to both force and the wave. Specifically, a decrease in the upper cutoff in frequency advances the start of the force prediction zone by increasing the slowest group velocity, while an increase in the lower cutoff in frequency pushes back the end of it, determined by the fastest group velocity. As a reminder, the two approaches for force prediction are equivalent in terms of resulting forces, and thus this investigation of the prediction zone is valid irrespective of the choice of method.

Lastly, depending on the response of the structure of interest, it is possible that the response prediction zone is larger than the wave prediction zone. This will occur when the FRF operates in different frequency ranges from the wave spectrum under consideration. While this topic is expected to be one feature utilized in practical prediction systems to optimize computational effort, it is not addressed in detail within this study.

4.3.3. Force prediction for multidirectional waves

In the multidirectional cases, the theoretical excitation forces $\eta_{ref} * h(t)$ are not obtainable since it is not possible to decompose the time series of surface elevation into the directional components with the phase information while the experimental data $f_{e,ref}(t)$ is available. Hence, we first simply demonstrate the algorithms' ability to extend to directional sea states by providing the resulting values for excitation force $f_{e,pred}(t)$ as well as the directional modes of excitation force $f_{e,n_\theta,pred}(t)$ across the prespecified directional bandwidth.

Fig. 16 presents individual directional components as well as the summation of directional components for the waves and forces. For the sake of compactness, we only present the results for one multidirectional case with moderate wave steepness and directional spreading (i.e. Case M2). In Case M2, every frequency component is divided into seven directional modes, symmetric about the main propagating direction 0°. The wave phases were chosen randomly from the same seed for both unidirectional and multidirectional cases, and thus the wave kinematics of cases are comparable. Consequently, different wave phases were used in Cases U2 and M2. As observed in Fig. 10, the relative amplitude of directional modes for excitation forces remains nearly the same compared to the corresponding modes for the surface waves. Therefore, the effect of propagating direction θ on the FRF and IRF appears to be relatively minor over $[-45°, 45°]$, and this is due to the geometry of the axisymmetric platform investigated in this study. In other words, the directionality may not need to be considered when calculating the excitation forces, while wave prediction requires consideration of directionality. Thus, we can hypothesize that the assumption of a unidirectional wave field is applicable for estimating the wave excitation forces for the structure's form and dimension as well as the wave parameters considered in the present study.

To validate the aforementioned hypothesis, we calculated simplified excitation forces using only the IRF of the main direction 0° (referred to as simplified forces in Fig. 17, $\eta_{ref} * h_{n_\theta}(t)$ with $n_\theta = \frac{N_\theta+1}{2}$). Fig. 17 compares these simplified results to the experimental ones $f_{e,ref}(t)$ and the predicted forces $f_{e,pred}(t)$ ($\eta_{pred} * h(t)$ or using a_n, b_n, and H_n). We note that the simplified forces indicated by the solid line in Fig. 17 should be distinguishable from the theoretical forces in the unidirectional cases shown in Fig. 11. The model predictions overall demonstrate great agreement with the simplified values and experimental data, thereby supporting the assumption made regarding the IRF for the specific condition considered here. As mentioned earlier for the unidirectional cases, the assumption on NEMOH (e.g., the linear interaction between wave and structure) and the measurement uncertainty may lead to deviations from the measured data. Similar results are obtained in the other cases (not shown here).

5. Conclusions

Kim et al. (2023a) developed phase-resolved ocean wave predictions to incorporate directional sea states and validated them against dedicated tank-scale experiments, considering sea states with different directional spreads. In the present study, we also considered additional wave conditions with varying wave steepnesses, and it was confirmed

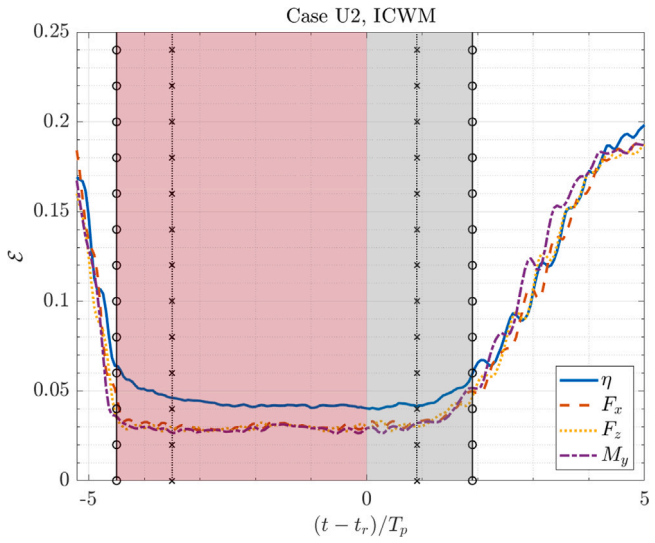

Fig. 15. Temporal evolution of prediction error by ICWM for Case U2 at WG21 (———: η; − − − −: F_x; ·····: F_z; —·—: M_y; solid-o: boundaries of wave prediction zone; dotted-x: boundaries of force prediction zone; red shading: nowcast; gray shading: forecast).

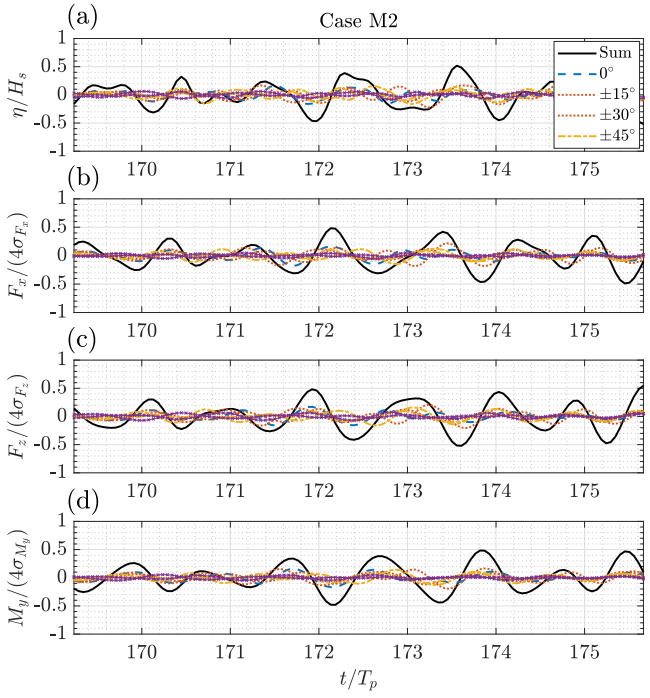

Fig. 16. Time series of decomposed surface elevation $\eta_{n_\theta,pred}$ and excitation force $f_{e,n_\theta,pred}$ for Case M2 at WG21: (a) η; (b) F_x; (c) F_z; (d) M_y (———: summation $\eta_{pred}(t)$ or $f_{e,pred}(t)$; − − − −: $\theta = 0°$; ·····: $\theta = \pm15°$; —·—: $\theta = \pm30°$; dash-x: $\theta = \pm45°$).

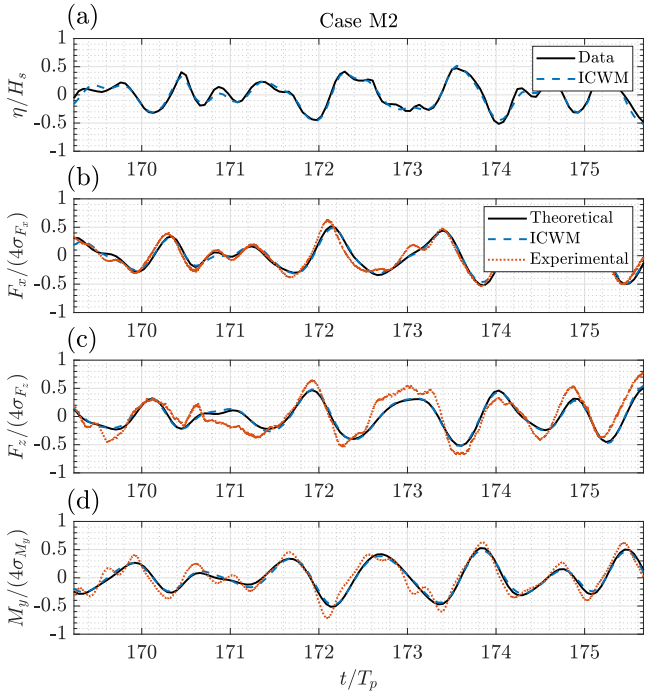

Fig. 17. Time series of surface elevation and excitation force for Case M2 at WG21: (a) η; (b) F_x; (c) F_z; (d) M_y (———: experimental waves $\eta_{ref}(t)$ in panel (a) and simplified forces $\eta_{ref} * h_{n_\theta}(t)$ with $n_\theta = \frac{N_\theta+1}{2}$ in panels (b), (c), and (d); − − − −: ICWM $f_{e,pred}(t)$ ($\eta_{pred} * h(t)$); ·····: experimental forces $f_{e,ref}(t)$).

that the wave prediction algorithms provide accurate descriptions of the ocean surface for all wave conditions, regardless of both wave steepnesses and directional spreads.

The excitation forces are generally calculated by implementing the convolution integral with impulse response functions in the time domain. As a concise alternative, we propose new frequency-domain approaches that directly apply initial wave conditions or wave amplitude parameters. This simplifies the force prediction process by eliminating certain steps involved in transforming between the time domain and frequency domain, such as simulating wave surfaces via wave propagation. Therefore, the novelty of this work lies in deriving a link between nonlinear wave models and linear wave-structure interaction in the frequency-domain method. Moreover, we conducted a study on the force prediction zone utilizing the theoretical forces, which are the linearized estimates via the BEM packages on the basis of the observed wave information at the point. This is the first time that the force prediction zone has been explored where the same prediction zone can be applied to both wave and force.

To verify the proposed excitation force estimation methods, we measured experimental excitation forces in both unidirectional and directional sea states. This was achieved by employing the captive

platform model that was excited by incident waves. The reasonable agreement between the force estimations and experimental results confirms the ability of the present methods to appropriately predict wave excitation forces under irregular wave fields. This work presents, for the first time, the validation of algorithms for predicting wave excitation force against the experimental data, especially in directional wave fields.

Finally, for the floating structure and the sea states investigated in this study, the assumption of unidirectionality when applying the boundary element method tools to compute excitation forces was justified. Because the structure of interest is simple and fairly small compared to the wavelengths considered and the spectral energy is primarily contained within a relatively narrow-angle range of $[-45°, 45°]$, the angular variability of the response function remains insignificant across this range.

CRediT authorship contribution statement

I.-C. Kim: Conceptualization, Investigation, Methodology, Software, Validation, Writing – original draft. **G. Ducrozet:** Project administration, Conceptualization, Methodology, Investigation, Writing – review & editing, Supervision. **V. Leroy:** Conceptualization, Methodology, Investigation, Writing – review & editing, Supervision. **F. Bonnefoy:** Conceptualization, Methodology, Investigation, Writing – review & editing, Supervision. **Y. Perignon:** Project administration, Conceptualization, Methodology, Investigation, Writing – review & editing, Supervision. **S. Delacroix:** Conceptualization, Methodology, Investigation.

Declaration of competing interest

The authors declare that they have no known competing financial interests or personal relationships that could have appeared to influence the work reported in this paper.

Data availability

Data such as experimental data sets and prediction results are openly available at https://doi.org/10.5281/zenodo.7689781 repository.

Acknowledgments

This work was done within the framework of the European H2020 FLOATECH project, Grant agreement ID: 101007142. The authors acknowledge the support of the French Agence Nationale de la Recherche (ANR), under grant ANR-20-CE05-0039 (project CREATIF).

The authors also thank the experimental team at LHEEA/Centrale Nantes-CNRS who contributed to the experimental campaign and the corresponding database.

References

Al, M., Fontanella, A., van der Hoek, D., Liu, Y., Belloli, M., van Wingerden, J.-W., 2020. Feedforward control for wave disturbance rejection on floating offshore wind turbines. In: Journal of Physics: Conference Series. IOP Publishing, 022048.

Babanin, A.V., Chalikov, D., Young, I., Savelyev, I., 2010. Numerical and laboratory investigation of breaking of steep two-dimensional waves in deep water. J. Fluid Mech. 644, 433–463.

Babarit, A., Delhommeau, G., 2015. Theoretical and numerical aspects of the open source BEM solver NEMOH. In: 11th European Wave and Tidal Energy Conference (EWTEC2015). pp. 08C1–1–1.

Bacelli, G., Coe, R.G., Patterson, D., Wilson, D., 2017. System identification of a heaving point absorber: Design of experiment and device modeling. Energies 10 (4), 472.

Blondel, E., Bonnefoy, F., Ferrant, P., 2010. Deterministic non-linear wave prediction using probe data. Ocean Eng. 37 (10), 913–926.

Bonnefoy, F., Delacroix, S., Ducrozet, G., Kim, I., Leroy, V., 2023. FLOATECH Project database. http://dx.doi.org/10.5281/zenodo.7689781, Funded by European Commission, project FLOATECH, grant 101007142.

Chen, Y., Guza, R., Elgar, S., 1997. Modeling spectra of breaking surface waves in shallow water. J. Geophys. Res.: Oceans 102 (C11), 25035–25046.

Cretel, J.A., Lightbody, G., Thomas, G.P., Lewis, A.W., 2011. Maximisation of energy capture by a wave-energy point absorber using model predictive control. IFAC Proc. Vol. 44 (1), 3714–3721.

Cummins, W., 1962. The Impulse Response Function and Ship Motions. Technical Report, David Taylor Model Basin, Washington DC.

Desmars, N., Bonnefoy, F., Grilli, S., Ducrozet, G., Perignon, Y., Guérin, C.-A., Ferrant, P., 2020. Experimental and numerical assessment of deterministic nonlinear ocean waves prediction algorithms using non-uniformly sampled wave gauges. Ocean Eng. 212, 107659.

Falnes, J., 1995. On non-causal impulse response functions related to propagating water waves. Appl. Ocean Res. 17 (6), 379–389.

Fusco, F., Ringwood, J.V., 2012. A simple and effective real-time controller for wave energy converters. IEEE Trans. Sustain. Energy 4 (1), 21–30.

Grilli, S.T., Guérin, C.-A., Goldstein, B., 2011. Oceanwave reconstruction algorithms based on spatio-temporal data acquired by a flash LiDAR camera. In: The Twenty-First International Offshore and Polar Engineering Conference. OnePetro, pp. 275–282.

Guérin, C.-A., Desmars, N., Grilli, S.T., Ducrozet, G., Perignon, Y., Ferrant, P., 2019. An improved Lagrangian model for the time evolution of nonlinear surface waves. J. Fluid Mech. 876, 527–552.

Guo, B., Patton, R., Jin, S., 2017. Identification and validation of excitation force for a heaving point absorber wave energy convertor. In: Proc. EWTEC. pp. 1–9.

Guo, B., Patton, R.J., Jin, S., Lan, J., 2018. Numerical and experimental studies of excitation force approximation for wave energy conversion. Renew. Energy 125, 877–889.

Hals, J., Falnes, J., Moan, T., 2011. Constrained optimal control of a heaving buoy wave-energy converter. J. Offshore Mech. Arct. Eng. 133 (1).

Hillis, A., Brask, A., Whitlam, C., 2020. Real-time wave excitation force estimation for an experimental multi-DOF WEC. Ocean Eng. 213, 107788.

Hilmer, T., Thornhill, E., 2015. Observations of predictive skill for real-time deterministic sea waves from the WaMoS II. In: OCEANS 2015-MTS/IEEE Washington. IEEE, pp. 1–7.

Kabel, T., Georgakis, C.T., Zeeberg, A.R., 2019. Mapping ocean waves using new LIDAR equipment. In: Proceedings of the Twenty-Ninth (2019) International Ocean and Polar Engineering Conference. nternational Society of Offshore and Polar Engineers, pp. 2258–2562.

Kim, I.-C., Ducrozet, G., Bonnefoy, F., Leroy, V., Perignon, Y., 2023a. Real-time phase-resolved ocean wave prediction in directional wave fields: Enhanced algorithm and experimental validation. Ocean Eng. 276, 114212.

Kim, I.-C., Ducrozet, G., Perignon, Y., 2023b. Development of phase-resolved real-time wave forecasting with unidirectional and multidirectional seas. In: ASME 2023 42nd International Conference on Ocean, Offshore and Arctic Engineering. American Society of Mechanical Engineers Digital Collection, V005T06A104.

Kim, I.-C., Kaihatu, J.M., 2022. A modified frequency distribution function of wave breaking-induced energy dissipation. J. Geophys. Res.: Oceans e2022JC018792.

Klein, M., Dudek, M., Clauss, G.F., Ehlers, S., Behrendt, J., Hoffmann, N., Onorato, M., 2020. On the deterministic prediction of water waves. Fluids 5 (1), 9.

Kurnia, R., Ducrozet, G., 2023. NEMOH: Open-source boundary element solver for computation of first- and second-order hydrodynamic loads in the frequency domain. Comput. Phys. Comm. 292, 108885.

Kusters, J., Cockrell, K., Connell, B., Rudzinsky, J., Vinciullo, V., 2016. FutureWaves™: A real-time Ship Motion Forecasting system employing advanced wave-sensing radar. In: OCEANS 2016 MTS/IEEE Monterey. IEEE, pp. 1–9.

Lee, C., Newman, J., 2013. WAMIT User Manual, Version 7.0. WAMIT Inc, Chestnut Hill, Massachusetts.

Leroy, V., Delacroix, S., Merrien, A., Bachynski-Polić, E., Gilloteaux, J.-C., 2022. Experimental investigation of the hydro-elastic response of a spar-type floating offshore wind turbine. Ocean Eng. 255, 111430.

Ma, Y., Sclavounos, P.D., Cross-Whiter, J., Arora, D., 2018. Wave forecast and its application to the optimal control of offshore floating wind turbine for load mitigation. Renew. Energy 128, 163–176.

Mase, H., Kirby, J.T., 1992. Hybrid frequency-domain KdV equation for random wave transformation. Coast. Eng. Proc. (23).

Mitsuyasu, H., Tasai, F., Suhara, T., Mizuno, S., Ohkusu, M., Honda, T., Rikiishi, K., 1975. Observations of the directional spectrum of ocean WavesUsing a cloverleaf buoy. J. Phys. Oceanogr. 5 (4), 750–760.

Naaijen, P., Van Oosten, K., Roozen, K., van't Veer, R., 2018. Validation of a deterministic wave and ship motion prediction system. In: International Conference on Offshore Mechanics and Arctic Engineering, Vol. 51272. American Society of Mechanical Engineers, V07BT06A032.

Nouguier, F., Grilli, S.T., Guérin, C.-A., 2013. Nonlinear ocean wave reconstruction algorithms based on simulated spatiotemporal data acquired by a flash LIDAR camera. IEEE Trans. Geosci. Remote Sens. 52 (3), 1761–1771.

Nouguier, F., Guérin, C.-A., Chapron, B., 2009. "Choppy wave" model for nonlinear gravity waves. J. Geophys. Res.: Oceans 114 (C9).

Perlin, M., Bustamante, M.D., 2016. A robust quantitative comparison criterion of two signals based on the Sobolev norm of their difference. J. Eng. Math. 101 (1), 115–124.

Pierson, Jr., W.J., 1961. Models of Random Seas Based on the Lagrangian Equations of Motion. Technical Report, NEW YORK UNIV BRONX SCHOOL OF ENGINEERING AND SCIENCE.

Pierson, Jr., W.J., Moskowitz, L., 1964. A proposed spectral form for fully developed wind seas based on the similarity theory of SA Kitaigorodskii. J. Geophys. Res. 69 (24), 5181–5190.

Raach, S., Schlipf, D., Sandner, F., Matha, D., Cheng, P.W., 2014. Nonlinear model predictive control of floating wind turbines with individual pitch control. In: 2014 American Control Conference. IEEE, pp. 4434–4439.

Yu, Z., Falnes, J., 1995. State-space modelling of a vertical cylinder in heave. Appl. Ocean Res. 17 (5), 265–275.

Zhang, C., Chen, Z., Zhao, C., Chen, X., Wei, Y., He, J., 2022a. Deterministic sea wave prediction based on least squares with regularization algorithm using coherent microwave radar. IEEE Trans. Geosci. Remote Sens..

Zhang, J., Zhao, X., Jin, S., Greaves, D., 2022b. Phase-resolved real-time ocean wave prediction with quantified uncertainty based on variational Bayesian machine learning. Appl. Energy 324, 119711.